

Observation of quantum turbulence in superfluid $^3\text{He-B}$ using reflection and transmission of ballistic thermal excitations

M.J. Jackson,^{1,2} D.I. Bradley,¹ A.M. Guénault,¹ R.P. Haley,¹ G.R. Pickett,¹ and V. Tsepelin^{1,*}

¹*Physics Department, Lancaster University, Lancaster, LA1 4YB, United Kingdom.*

²*Faculty of Mathematics and Physics, Charles University,
Ke Karlovu 3, 121 16, Prague 2, Czech Republic.*

We report measurements of quantum turbulence generated by a vibrating grid in superfluid $^3\text{He-B}$ at zero pressure in the zero temperature limit. Superfluid flow around individual vortex lines Andreev-reflects incoming thermal ballistic quasiparticle excitations, and allows non-invasive detection of quantum vortices in $^3\text{He-B}$. We have compared two Andreev reflection-based techniques traditionally used to detect quantum turbulence in the ballistic regime: quasiparticle transmission through and reflection from ballistic vortex rings and a turbulent tangle. We have shown that the two methods are in very good agreement and thus complement each other. Our measurements reveal that vortex rings and a tangle generated by a vibrating grid have a much larger spatial extent than previously realised. Furthermore, we find that a vortex tangle can either pass through an obstacle made from a mesh or diffuse around it. The measured dependence of vortex signal as a function of the distance from the vibrating grid is consistent with a power-law behaviour in contrast to turbulence generated by a vibrating wire which is described by an exponential function.

PACS numbers: 67.30.H-, 67.30.he, 67.30.em

Quantum turbulence in the zero temperature limit shares many of the general properties of its classical counterpart but is conceptually much simpler, being a tangle of singly quantised vortex lines in an incompressible fluid that possesses no viscous dissipation¹. Quantum turbulence has been observed in superfluid ^4He ^{2,3}, superfluid $^3\text{He-B}$ ⁴⁻⁶ and in Bose-Einstein condensates⁷, where the emergence of a turbulent cascade was recently observed⁸. The research of quantum turbulence in different systems is complementary, since various properties can be addressed and compared. The strength of superfluid $^3\text{He-B}$ lies in the ability to probe a turbulent tangle non-invasively using the condensate's own thermal excitations (quasiparticles and quasiholes)^{9,10}. At low temperatures, the mean free path of excitations exceeds the confines of any experimental volume and, in this ballistic regime, the excitations move independently. In addition to normal scattering, excitations can also undergo Andreev reflection¹¹, which is unique to Fermi condensates and underpins the detection of quantised vortices in superfluid $^3\text{He-B}$.

The dispersion curve $E(\mathbf{p})$ of excitations with momentum \mathbf{p} undergoes a Galilean transformation $E(\mathbf{p}) + \mathbf{p} \cdot \mathbf{v}$ in the presence of superfluid flow with velocity \mathbf{v} and governs the detection of quantum vortices¹². The direction of the flow determines whether quasiparticles or quasiholes incident on a velocity field will pass through or will be Andreev retro-reflected if the energy barrier arising due to the flow, $\Delta + \mathbf{p} \cdot \mathbf{v}$, is sufficiently high (Δ is the superfluid energy gap). At temperatures below 100 μK and at zero pressure, the scattering diameter of vortices for Andreev reflection is 6.3 μm ⁹, which significantly exceeds the superfluid coherence length, $\xi_0 \sim 50$ nm. A similar picture is observed at 29 bar pressure¹³, therefore observing vortices in superfluid $^3\text{He-B}$ at low temperatures is relatively straightforward. Two detection techniques are

available: transmission and reflection.

Transmission-based detection uses a reduction in the density of excitations behind the vortices (a quasiparticle “shadow”). A comparison is made between an incident quasiparticle flux scattered from an oscillating object in the presence and absence of quantum vortices⁵. This technique has allowed turbulence at different distances from the source of quantum vortices to be observed^{14,15}, as well as the statistical properties of fluctuations in the steady state and the cross-correlation between various detectors to be measured^{9,10,16}. The main advantages of the transmission techniques are speed and scalability, since multiple detectors can be placed in a turbulent region.

In addition to the creation of a “shadow” behind the quantum vortices, the Andreev process nearly perfectly retro-reflects incoming excitations back to their source, by converting quasiparticles to quasiholes and *vice versa* with negligible momentum transfer¹⁷. Reflection techniques measure the fraction of quasiparticles returned back into a bolometrically-calibrated source of quasiparticles, known as a black box radiator (BBR)¹⁸. Reflection-based detection has been used to observe superfluid flow around a paddle,¹⁹ a turbulent tangle^{20,21} and an array of rectilinear vortices¹³. The bolometric technique has been successfully applied to quantum vortices produced inside the BBR in order to study the energy decay of turbulence²² and propagation of a rotating vortex front²³.

In this manuscript, we use both transmission and reflection techniques to probe quantum vortices in the same region of our experimental volume. Quantum turbulence was generated by a vibrating grid resonator and detected by several vibrating wires and two BBRs. Our results show that the two methods give virtually identical fractional screening (the amount of Andreev reflection) and

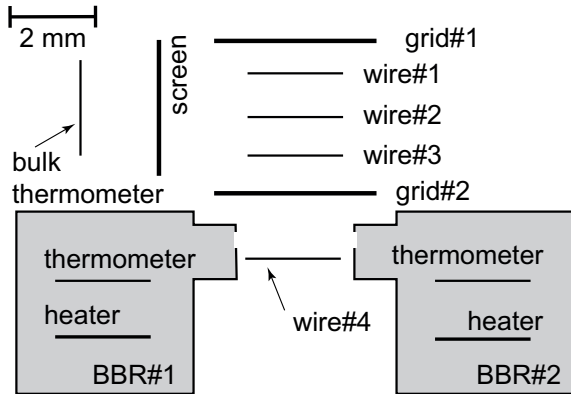


FIG. 1: Schematic diagram of the experimental volume showing the mechanical oscillators used in our measurements. For details, see text.

thus complement each other. Our measurements are consistent with a recent theoretical result predicting a similar amount of Andreev reflection at low temperatures using “particle” and “energy” flux, which correspond to transmission and reflection techniques, respectively²⁴.

All measurements described here were performed in superfluid $^3\text{He-B}$ at temperatures below $0.2T_c$ and at zero pressure. The ^3He is cooled by a Lancaster-style nuclear cooling stage²⁵ mounted on the Lancaster Advanced Nuclear Cooling Refrigerator²⁶. The experimental arrangement used is illustrated in Fig. 1.

Turbulence was generated using the vibrating grid resonator labeled grid#1, and was detected using the vibrating wire resonators shown. Grid#1 consists of a $125\ \mu\text{m}$ diameter tantalum wire bent into a $5\ \text{mm}$ square with a $5.1 \times 3.5\ \text{mm}$ copper mesh glued to it using GE varnish. The mesh has $22.6\ \mu\text{m}$ square holes with a periodicity of $34.5\ \mu\text{m}$. The vibrating wire resonators are $2.5\ \text{mm}$ diameter loops of $4.5\ \mu\text{m}$ NbTi filament made from multifilament superconducting wire²⁷. Three wire detectors, #1, #2 and #3, in the figure were positioned directly behind grid#1 at distances $1.5\ \text{mm}$, $2.4\ \text{mm}$ and $3.5\ \text{mm}$, respectively. A fourth detector, wire#4 was placed roughly $5.8\ \text{mm}$ away from grid#1, and is located behind a second grid, grid#2, between two BBRs that face each other. Unfortunately, grid#2 could not produce turbulence due to a large intrinsic damping and the results presented here will only focus on measurements using grid#1 (below, we will often refer to grid#1 simply as “the grid”). The BBRs consist of a small box made from Stycast-impregnated paper of dimensions $4 \times 4 \times 4\ \text{mm}$ with a cylindrical turret of volume $\sim 2\ \text{mm}^3$. Each BBR contains two vibrating wire resonators¹⁸; a $13\ \mu\text{m}$ wire which acts as a heater and a $4.5\ \mu\text{m}$ wire which acts as a thermometer. The turrets of the BBRs are separated by $3\ \text{mm}$ and have a $0.3\ \text{mm}$ aperture which acts as a weak thermal link between the superfluid inside the box and the bulk outside. Both apertures are aligned and located roughly $5.3\ \text{mm}$ away from grid#1 at the same height as the apex of wire#4. The bulk thermometer wire was placed to a

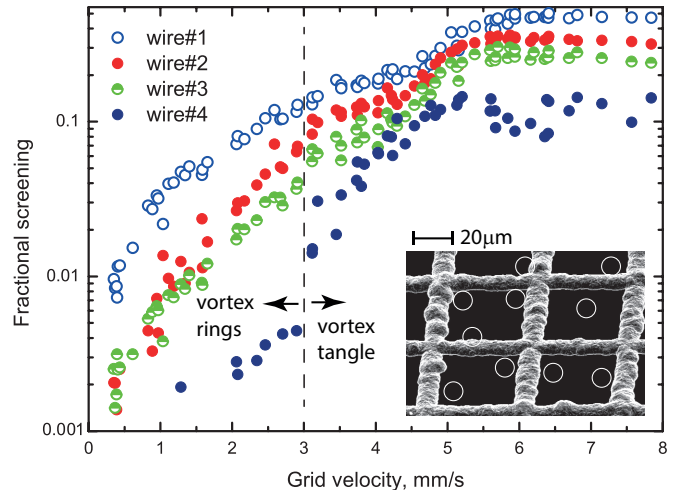


FIG. 2: (Color online.) Log-linear plot of the fractional screening measured by the four wire detectors as a function of the peak grid velocity at zero pressure over the temperature range $0.17\text{--}0.19T_c$. The vertical dashed line shows the approximate grid velocity where vortex rings entangle and produce quantum turbulence. The insert contrasts a representation of $10\ \mu\text{m}$ diameter vortex rings and a micrograph of grid#2, which separates wire#4 from the source of turbulence and other detectors. See text for details.

side of the grid and behind a screen to shield it from turbulence.

We first measured the extent of turbulence generated by the grid using the transmission technique. The methodology and technical details were similar to those described elsewhere⁹. Figure 2 presents fractional screening produced by quantum vortices as a function of the grid velocity, as detected by the four vibrating wires. Our measurements show that the fractional screening rises rapidly with grid velocity up to $\sim 5.5\ \text{mm s}^{-1}$ and then appears to saturate, becoming independent of the grid velocity. The significant heating accompanying turbulence production at large grid velocities may cause this saturation and is responsible for the large scatter on wire#4.

We know from previous measurements,^{9,28,29} that the grid produces ballistic vortex rings at low velocities (below $\sim 3\ \text{mm s}^{-1}$). As grid velocity increases, so does the density of these rings, increasing the probability of interactions and reconnections which form the vortex tangle. The vertical dashed line on Fig. 2 marks the approximate position where the grid starts to produce a vortex tangle. Usually, the fractional screening does not carry information about vortex types, as evidenced by the measurements on wires#1, #2 and #3. However, the fractional screening detected by wire#4 shows a clear transition at this grid velocity, and indicates that the fractional screening due to the tangle is larger than that due to the vortex rings. The observed result is unexpected since wire#4 is located behind grid#2, which should stop or at least impede the propagation of any turbulence. The diameter of the ballistic vortex rings produced by grid#1

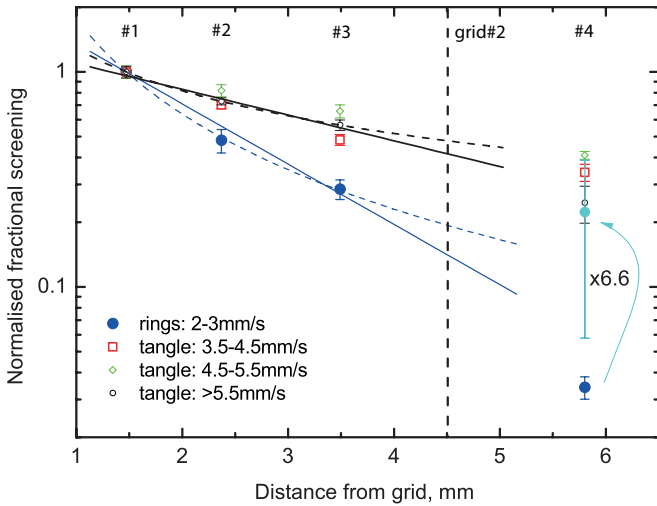


FIG. 3: (Color online.) The normalised fractional screening, averaged over a range of grid velocities, as a function of distance from the grid. The solid and dashed lines correspond to least-square fitting of normalised fractional screening measured by wires #1, #2 and #3 using exponential and power-law functions, respectively. The cyan filled circle shows the expected response of wire#4 in the absence of grid#2, whose location is shown as the vertical dashed line. See text for details.

is velocity independent and equals $10 \pm 5 \mu\text{m}^9$. Grid#2 is made from $11 \mu\text{m}$ diameter wire with a periodicity of $34.5 \mu\text{m}$, and we estimate that a flux of $10 \mu\text{m}$ diameter rings will be attenuated by a factor of about 7 as they pass through it. The insert of Fig. 2 illustrates a micrograph of the mesh used to manufacture grid#2 and rings with a $10 \mu\text{m}$ diameter. For a tangle, the expected reduction of fractional screening behind grid#2 should be significantly larger compared to the ballistic rings, since larger vortex structures should be captured by the grid's mesh. In fact, we were very surprised to find that *any* signal from the vortex tangle from grid#1 could be observed behind grid#2. To produce a significant vortex signal on wire#4, the turbulence from grid#1 must diffuse around the top and bottom of grid#2 as the space to the sides of grid#2 are obstructed by the two BBRs. Another possibility is that the turbulent tangle is pushed through the mesh, or creates further quantised vortices on the grid#2 due to its small but observable mean propagation velocity⁹ of 0.3 mm s^{-1} to 0.9 mm s^{-1} . The mean tangle velocity was deduced⁹ using the cross-correlation of fractional screening between pairs of wires #1, #2 and #3. The presence of turbulence behind grid#2 should be investigated further by placing a detector inside a mesh cage in front of a source of vortices.

Figure 3 shows the fractional screening detected on the different wires normalised by the fractional screening of wire#1 as a function of the distance between the detector wire and the turbulent source, grid#1. The data was obtained by averaging measurements presented in Fig. 2 for several grid velocities and compares the frac-

tional screening resulting from ballistic rings and a turbulent tangle. The normalised fractional screening for tangles produced at different grid velocities are clustered together. Figure 3 allows us to extract information on the spatial profile for vortex rings and a turbulent tangle along the direction of motion. A theoretical calculation of the fractional screening as a function of distance from a turbulent source does not exist, but we expect it to decrease exponentially as $f \propto \exp(-x/d_0)$ with increasing distance x from the grid, similarly to previous zero pressure measurements¹⁴, where turbulence was generated by a vibrating wire resonator and d_0 was found to be $\approx 2 \text{ mm}$. At 12 bar pressure, the spatial extent of the turbulence generated by another grid was estimated to be $\approx 1.5 \text{ mm}$, using only two detector wires located approximately 1 mm and 2 mm from the grid¹⁵. In this earlier measurement, the steady state vortex signal was roughly a factor of two smaller on the furthest wire, while the present measurements reveal that the fractional screening from wire#2 is $\sim 50\%$ and $\sim 30\%$ smaller than that from wire#1 for the vortex rings and turbulent tangle, respectively.

In Fig. 3, we show the least-square fitting of the normalised fractional screening measured by wires #1, #2 and #3 for vortex rings and for a tangle using exponential and power-law functions. The furthest wire, wire#4, was excluded from the fitting as it is located behind grid#2. Figure 3 includes the expected wire#4 signal for vortex rings by scaling the measured response using the grid attenuation calculated above. The straight blue solid line corresponds to an exponential variation of the vortex ring signal with $d_0 = 1.5 \pm 0.2 \text{ mm}$. The dashed blue line represents the power-law behaviour $f \propto x^{-1.5}$ and seems to fit the rings data better. It also shows the correct tendency towards the extrapolated response of wire#4.

The tangle data for grid velocities above 5.5 mm s^{-1} was chosen as representative and analysed similarly to the rings data. Fitting of the vortex signal yielded the extent of turbulence to be $d_0 = 3.6 \pm 0.6 \text{ mm}$ for an exponential variation and a power-law behaviour $f \propto x^{-0.66}$. The power-law functional dependence may fit our data slightly better, but the difference is less pronounced compared to the vortex rings data. If the generated tangle diffuses around grid#2, the inferred location of wire#4 should be 3 mm to 4 mm farther than its actual position and further supports a power-law dependence. Measurements conducted at 4.3 bar pressure in this experimental cell yield a similar extent of turbulence with $d_0 = 3.4 \pm 0.6 \text{ mm}$ for an exponential variation of the vortex signal and a power law behaviour $f \propto x^{-0.68}$. It is clear that theoretical calculations and numerical simulations are required to find the actual functional dependence of fractional screening. Regardless of the explicit functional dependence, our measurements show that the turbulence generated by a vibrating grid in $^3\text{He-B}$ at low pressure has a long tail, extending over much larger distances than previously realised. Furthermore, the cell parts desired to be free of turbulence require more rigor-

ous protection than a simple obstacle or a partial mesh partition.

The large spatial extent of the vortex tangle allowed us to contrast quantum vortices measured by wire#4 and the BBRs. Prior to turbulence measurements, we calibrated both BBRs and observed that they emit and receive quasiparticle beam as expected. The quasiparticle density inside the radiator volume was increased using the $13\mu\text{m}$ heater wire in order to produce a quasiparticle beam with intensity greater than that of the ambient quasiparticles. The quasiparticles produced travel ballistically and thermalise by scattering off the inside walls of the radiator before leaving through the aperture. In equilibrium, the power carried away by the quasiparticle beam equals the power entering the radiator from all sources¹²

$$\dot{Q}_{\text{beam}} = \dot{Q}_{\text{tot}} = \dot{Q}_{\text{wall}} + \dot{Q}_{\text{ext}} + \dot{Q}_{\text{app}} \quad (1)$$

where \dot{Q}_{wall} is the heat leak into the radiator volume from the paper walls of the box, \dot{Q}_{ext} is the heat leak due to the ambient thermal quasiparticles in the surrounding bulk superfluid and \dot{Q}_{app} is the power applied to the heater, given by the product of the drive current and the signal voltage.

The power emitted by the beam $\dot{Q}_{\text{beam}} = \frac{1}{2}\langle nv_g \rangle \tilde{E}_T A$ is a function of the quasiparticle flux inside the radiator $\langle nv_g \rangle$, the effective area of the aperture A and the mean thermal quasiparticle energy $\tilde{E}_T = \Delta + k_B T$ at temperature T . The thermal damping of the thermometer wire (width of the resonant peak) Δf_2^T inside the radiator can be used to infer the quasiparticle flux and to determine the power emitted by the beam²⁰

$$c\dot{Q}_{\text{beam}} = \Delta f_2^T \tilde{E}_T T = W. \quad (2)$$

Here c is termed the ‘‘box calibration constant’’ and $\Delta f_2^T \tilde{E}_T T$ is a quantity we call the ‘‘width parameter’’ W .

The calibration of the BBRs was carried out by continuously monitoring the width of thermometer wires in the BBRs and in bulk superfluid while $\sim 100\text{s}$ long heating pulses of known power were applied to the BBR heater wire. During the pulse, the change in the thermal damping of the heated box’s thermometer wire is measured and converted into a width parameter. The change in the bulk thermometer’s width parameter is subtracted from the latter to account for the external power entering the radiator.

Figure 4 shows the calibration of both BBRs obtained by applying a known amount of power and measuring the change in the box width parameter $\delta W = \delta \Delta f_2^T \tilde{E}_T T$. The open data points in Fig. 4 correspond to the BBRs that are heated and emit the quasiparticle beam, while closed points show the change of the width parameter in unheated BBRs that receive a fraction of the incoming quasiparticle beam. The change in the width parameter is found to be directly proportional to the applied power over several orders of magnitude for both BBRs.

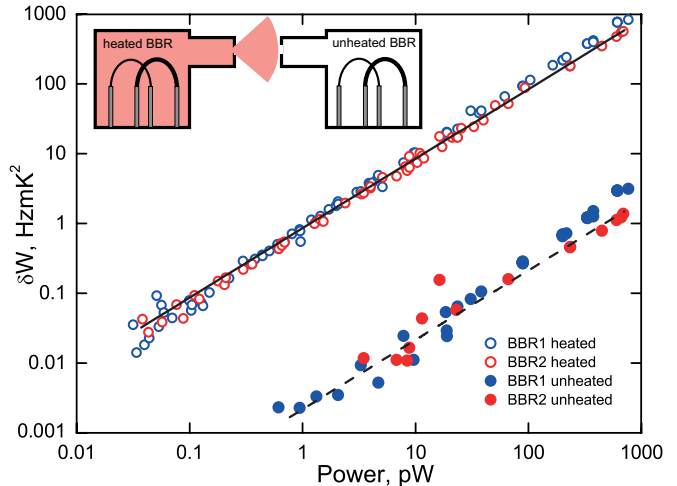


FIG. 4: (Color online) Change of width parameter $\delta \Delta f_2^T \tilde{E}_T T$ for both BBRs as a function of applied power, where T and \tilde{E}_T are in units of mK using the Greywall temperature scale³⁰. The open and closed symbols correspond to the change of width parameter of the heated (under calibration) and unheated (receiving beam from the heated box) BBRs correspondingly. The heat leak from the walls into the BBR, \dot{Q}_{wall} , is estimated to be $\leq 25\text{ fW}$. The straight solid line is least-squares fit with a gradient of unity, which yields the box calibration constant $c = 85\text{ Hz mK}^2\text{ pW}^{-1}$. The dashed line corresponds to the expected fraction of the received quasiparticle beam, and agrees very well with measurements. For details, see text.

A simple calculation in the framework of kinetic theory suggests that the fraction of the quasiparticle beam received by the opposite BBR is R_{app}^2/D^2 , where R_{app} is the radius of the BBR’s aperture and D is the distance between the BBR apertures. In our experimental cell, the aperture radius is 0.15 mm and the distance between the BBR turrets is 3 mm , which results in an expected fraction of 0.25% . The dashed straight line in Fig. 4 corresponds to the calculated fraction and is in excellent agreement with our measurements.

When the source of turbulence is switched on, a fraction of quasiparticles f will be Andreev-reflected and will retrace their original trajectories back into the BBR, regardless of the angle of incidence on the velocity field of quantum vortices. The energy balance of the outgoing beam should thus contain an extra term $f\dot{Q}_{\text{beam}}$, corresponding to the power returned to the box²⁰

$$\dot{Q}_{\text{beam}} = \dot{Q}_{\text{wall}} + \dot{Q}_{\text{ext}} + \dot{Q}_{\text{app}} + f\dot{Q}_{\text{beam}}. \quad (3)$$

During turbulence production, the generator causes extra heating outside the BBR and this is accounted for by using the \dot{Q}_{ext} term. The fractional screening f can be obtained by rewriting Eq. (3) in terms of the measured width parameters²⁰

$$f = 1 - \frac{\dot{Q}_{\text{app}}^{\text{on}}}{\dot{Q}_{\text{app}}^{\text{off}}} \frac{W_{\text{heat}}^{\text{off}} - W_{\text{noheat}}^{\text{off}}}{W_{\text{heat}}^{\text{on}} - W_{\text{noheat}}^{\text{on}}}, \quad (4)$$

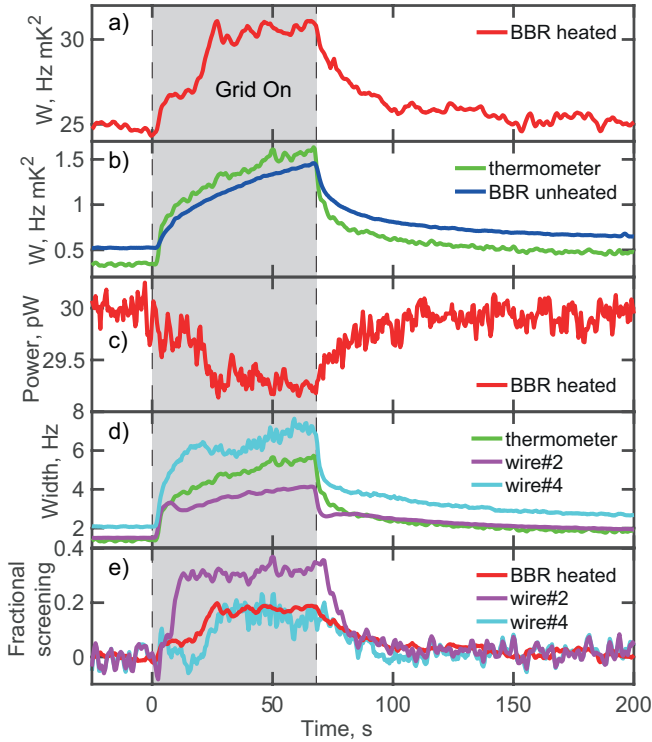


FIG. 5: (Color online) Comparison of turbulence measurements using reflection and transmission techniques during a typical grid pulse. The light grey area corresponds to the time when the grid is switched on and produces turbulence. The grid velocity is 5.6 mm s^{-1} . **a)** Width parameter of heated BBR. **b)** Width parameters of unheated BBR and the bulk thermometer. **c)** The variation of applied power \dot{Q}_{app} during the creation of turbulence. **d)** Change of damping experienced by the bulk thermometer and detector wires #2 and #4. **e)** Fractional screening measured by reflection (BBR) and transmission (wires #2 and #4) techniques during a grid pulse.

where $W_{\text{heat}}^{\text{off}}$ ($W_{\text{heat}}^{\text{on}}$) is the width parameter inside the heated radiator before (during) the generation of quantum vortices, and $W_{\text{noheat}}^{\text{off}}$, $W_{\text{noheat}}^{\text{on}}$ are the width parameters of the same BBR when it is unheated and does not emit a quasiparticle beam. The ratio $\dot{Q}_{\text{app}}^{\text{on}}/\dot{Q}_{\text{app}}^{\text{off}}$ accounts for the reduction of heating power applied to the BBR since the heater wire under a constant driving force slows down due to increased damping associated with the temperature increase inside the BBR.

Figure 5 compares the detection of a turbulent tangle using the reflection and transmission techniques for a grid velocity of 5.6 mm s^{-1} . The grid was turned on for a duration of $\sim 67 \text{ s}$, which is highlighted by the grey area in the figure. The temporal variation of the width parameter for the BBR emitting a quasiparticle beam is shown in Fig. 5a). The time trace of the width parameter of the unheated BBR and a bulk thermometer are illustrated in Fig. 5b). The width parameters of all detectors increased after the grid was turned on due to the overall heating of the cell. The change of width param-

eter of the heated BBR is significantly larger compared to the thermometer and unheated BBR, and indicates that part of the emitted beam is retro-reflected back into the BBR. Figure 5c) illustrates the reduction of the power applied to the BBR heater during turbulence production. The applied power, product of a constant force driving the heater wire and wire velocity, decreased approximately 3% due to the temperature increase inside the BBR, which caused by a part of the outgoing beam being Andreev reflection back into BBR.

The temporal variation of the damping experienced by the detector wires #2, #4 and the bulk thermometer are shown in Fig. 5d). A comparison of wire#2 and the bulk thermometer nicely demonstrates the arrival of a vortex tangle at the detector; the measured width of the detector wire becomes smaller than that of the thermometer, which is only possible due to screening. Since wire#4 is located further away behind another grid and is slightly heated by the BBR beam, its width reduction is more subtle and the time taken for the turbulent tangle to reach it is longer.

Figure 5e) contrasts the fractional screening obtained by reflection (BBR) and transmission (wire#4) measurements and demonstrates that in the steady state, the results are similar. After the grid was switched off and the tangle started to decay, both methods agree well with each other. The time traces of the BBR and wire#4 during the development of turbulence differ slightly, and could be caused by the difference in time constants of the BBR and detector, by the change of power leaving the BBR during the formation of the tangle, or perhaps by the relatively high noise in our measurements at this grid velocity. We note that 5.6 mm s^{-1} is the highest grid velocity where we observed a good agreement between both methods. Despite a slight variation between the signals, both methods show signs of the initial arrival of vortex rings and a gradual build up of the tangle. The overall picture resembles the data presented in Ref⁹, where the propagation velocity of quantum vortices was studied in detail.

Figure 6 summarises the dependence of fractional screening as a function of grid velocity measured using both techniques. The data shows that the reflection and transmission measurements are in very good agreement until the grid velocity reaches approximately 6 mm s^{-1} , where the heating accompanying turbulence production becomes large. Our observations show that both techniques result in similar fractional screening for the ballistic rings emitted by the grid below $\sim 3 \text{ mm s}^{-1}$ and the tangle at higher velocities. The obtained result is consistent with theoretical calculations predicting that at low temperatures the “particle” flux (transmission) and the “energy” flux (reflection) measurements should detect a similar amount of Andreev reflection²⁴. We can conclude that both the reflection and transmission techniques complement each other and can now be used to study different aspects of turbulence in superfluid $^3\text{He-B}$. At the highest grid velocities, the scatter in fractional

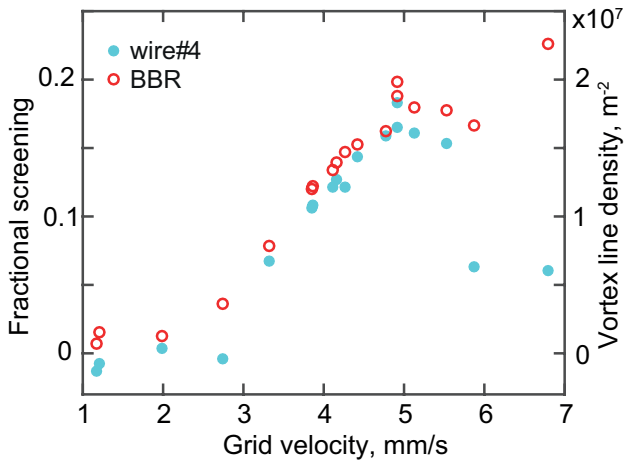


FIG. 6: (Color online) Comparison of fractional screening measured using transmission (wire#4) and reflection (BBR) techniques as a function of the grid's velocity. Both data sets are in very good agreement. The right axis shows the approximate vortex line densities inferred using a simple 1D model which assumes that the tangle is homogeneous using Eq. (11) from Ref⁹. For the details, see text.

screening is substantial (see Fig. 2, wire#4), and to conclude which of two methods is more accurate and precise new measurements with a vibrating wire detector and a BBR located next to the turbulence source are required. Ideally, they should be carried out over a wide temperature range in a rotating cryostat where the number of quantum vortices is known¹³. Care should be taken to shield thermometry resonators, since the extent of turbulence generated by the vibrating grid at zero pressure is nearly twice as big as previously thought. In addition, we have observed the transmission of quasiparticles from one BBR into another and found it to be consistent with the ballistic transport model.

We thank A. Stokes and M. G. Ward for excellent technical support. This research is supported by the UK EPSRC grants No. EP/L000016/1, No. EP/I028285/1 and the European FP7 Program MICROKELVIN Project 228464. M.J.J. also acknowledges support by the Czech Science Foundation project GAČR 17-03572S.

All data used in this paper are available at <http://dx.doi.org/10.17635/lancaster/researchdata/135>, including descriptions of the data sets.

* v.tsepelin@lancaster.ac.uk

- ¹ C.F. Barenghi, L. Skrbek and K.R. Sreenivasan, *Proc. Natl. Acad. Sci. U.S.A.* **111**, 4649 (2014).
- ² W.F. Vinen and J.J. Niemela, *J. Low. Temp. Phys.* **128** 167 (2002).
- ³ R.J. Donnelly, *Quantized Vortices in Helium II*, Cambridge University Press, Cambridge, 1991.
- ⁴ S.N. Fisher, A.M. Guénault, A.J. Hale and G.R. Pickett, *J. Low. Temp. Phys.* **121** 393 (2000).
- ⁵ S.N. Fisher, A.J. Hale, A.M. Guénault and G.R. Pickett, *Phys. Rev. Lett.* **86**, 244 (2001).
- ⁶ A.P. Finne, T. Araki, R. Blaauwgeers, V.B. Eltsov, N.B. Kopnin, M. Krusius, L. Skrbek, M. Tsubota and G.E. Volovik, *Nature* **424** 1022 (2003).
- ⁷ E.A.L. Henn, J.A. Seman, G. Roati, K.M.F. Magalhães and V.S. Bagnato, *Phys. Rev. Lett.* **103** 045301 (2009).
- ⁸ N. Navon, A.L. Gaunt, R.P. Smith and Z. Hadzibabic, *Nature* **539** 72 (2016).
- ⁹ S.N. Fisher, M.J. Jackson, Y.A. Sergeev and V. Tsepelin, *Proc. Natl. Acad. Sci. U.S.A.* **111**, 4659 (2014).
- ¹⁰ A.W. Baggaley, V. Tsepelin, C.F. Barenghi, S.N. Fisher, G.R. Pickett, Y.A. Sergeev, and N. Suramlishvili, *Phys. Rev. Lett.* **115**, 015302 (2015).
- ¹¹ A.F. Andreev, *Sov. Phys. JETP* **19**, 1228 (1964).
- ¹² S.N. Fisher, in *Vortices and Turbulence at Very Low Temperatures*, CISM Courses and Lectures Vol. 501, edited by C.F. Barenghi and Y.A. Sergeev (Springer, Wien-New York, 2008), p. 177
- ¹³ J.J. Hosio, V.B. Eltsov, R. de Graaf, M. Krusius, J. Mäkinen, and D. Schmoranzler, *Phys. Rev. B* **84**, 224501 (2011).
- ¹⁴ D.I. Bradley, S.N. Fisher, A.M. Guénault, M.R. Lowe, G.R. Pickett and A. Rahm, *Physica B* **329**, 104 (2003).
- ¹⁵ D.I. Bradley, D.O. Clubb, S.N. Fisher, A.M. Guénault,

R.P. Haley, C.J. Matthews, G.R. Pickett, V. Tsepelin and K. Zaki, *Phys. Rev. Lett.* **96**, 035301 (2006).

- ¹⁶ D.I. Bradley, S.N. Fisher, A.M. Guénault, R.P. Haley, S. O'Sullivan, G.R. Pickett and V. Tsepelin, *Phys. Rev. Lett.* **101**, 065302 (2008).
- ¹⁷ C.F. Barenghi, Y.A. Sergeev, and N. Suramlishvili, *Phys. Rev. B* **77**, 104512 (2008).
- ¹⁸ S.N. Fisher, A.M. Guénault, C.J. Kennedy and G.R. Pickett, *Phys. Rev. Lett.* **69**, 1073 (1992).
- ¹⁹ M.P. Enrico, S.N. Fisher, A.M. Guénault, G.R. Pickett and K. Torizuka, *Phys. Rev. Lett.* **70**, 1846 (1993).
- ²⁰ D.I. Bradley, S.N. Fisher, A.M. Guénault, M.R. Lowe, G.R. Pickett, A. Rahm and R.C.V. Whitehead, *Phys. Rev. Lett.* **93**, 235302 (2004).
- ²¹ J.J. Hosio, V.B. Eltsov, M. Krusius, J.T. Mäkinen, *Phys. Rev. B* **85** 224526 (2012).
- ²² D.I. Bradley, S.N. Fisher, A.M. Guénault, R.P. Haley, G.R. Pickett, D. Potts, and V. Tsepelin, *Nature Phys.*, **7** 473 (2011).
- ²³ J.J. Hosio, V.B. Eltsov, R. de Graaf, P.J. Heikkinen, R. Hänninen, M. Krusius, V.S. L'vov, and G.E. Volovik, *Phys. Rev. Lett.* **107**, 135302 (2011).
- ²⁴ Y.A. Sergeev, C.F. Barenghi, S.N. Fisher, V. Tsepelin and N. Suramlishvili, *Phys. Rev. B* **91**, 134507 (2015).
- ²⁵ G.R. Pickett and S.N. Fisher, *Physica B* **329** 75 (2003).
- ²⁶ D.J. Cousins, S.N. Fisher, A.M. Guénault, R.P. Haley, I.E. Miller, G.R. Pickett, G.N. Plenderleith, P. Skyba, P.Y.A. Thibault and M.G. Ward, *J. Low Temp. Phys.* **114**, 547 (1999).
- ²⁷ A.M. Guénault, V. Keith, C.J. Kennedy, S.G. Mussett and G.R. Pickett, *J. Low Temp. Phys.* **62**, 511 (1986).
- ²⁸ D.I. Bradley, D.O. Clubb, S.N. Fisher, A.M. Guénault, R.P. Haley, C.J. Matthews, G.R. Pickett, V. Tsepelin and K.L. Zaki, *Phys. Rev. Lett.* **95**, 035302 (2005).

²⁹ S. Fujiyama, A. Mitani, M. Tsubota, D.I. Bradley, S.N. Fisher, A.M. Guénault, R.P. Haley, G.R. Pickett and V. Tsepelin, *Phys. Rev. B* **81**, 180512 (2010).

³⁰ D.S. Greywall, *Phys. Rev. B* **33**, 7520 (1986).